Physics of Plasmas ARTICLE scitation.org/journal/php

Suppression of single-surface multipactor discharges due to non-sinusoidal transverse electric field

Cite as: Phys. Plasmas **26**, 093503 (2019); doi: 10.1063/1.5111734
Submitted: 29 May 2019 · Accepted: 9 August 2019 ·
Published Online: 6 September 2019

De-Qi Wen,[1] Asif Iqbal,[1] Peng Zhang,[1] and John P. Verboncoeur[1,2]

AFFILIATIONS

[1]Department of Electrical and Computer Engineering, Michigan State University, East Lansing, Michigan 48824, USA
[2]Department of Computational Mathematics, Science and Engineering, Michigan State University, East Lansing, Michigan 48824, USA

ABSTRACT

It is of importance to suppress single-surface multipactor discharges in high power microwave devices. In this work, both particle-in-cell (PIC) and Monte-Carlo simulations demonstrate that multipactor discharges can be significantly suppressed by a temporal Gaussian-type transverse electric field waveform. Decreasing the half peak width of the Gaussian electric field can reduce the time-averaged positive charge density on the surface, corresponding to the strength of the multipactor, by an order of magnitude at fixed time-averaged input power. The underlying physical mechanism is revealed by examining the electron impact energy and angle distribution in detail, as well as the dynamic secondary electron yield (SEY) from PIC simulation. For the smaller half peak width and fixed average input power, more electrons striking the surface have energies either below the first crossover or higher than the second crossover of the SEY curve, giving rise to weaker secondary electrons emission and finally resulting in a weaker multipactor discharge. In addition, we give the analytical expressions of the frequency spectrum and phase shift needed to recover a Gaussian-type waveform, which is in excellent agreement with numerical calculations.

I. INTRODUCTION

Multipactor discharges near dielectric windows are frequently observed in a multitude of devices, such as high power microwave transmission devices[1–7] and space-based communication systems. In such a multipactor discharge, the primary electrons mainly obtain energy from the radio frequency electric field and return to the dielectric surface by the restoring surface field. The secondary electron emission (SEE) depends on the impact energy, impact angle, and material characteristics. When the rf period-averaged secondary electron yield (SEY) is larger than unity, the multipactor will grow until the restoring field is strong enough to reduce the hop time, and consequently, the rf period-averaged SEY equals unity. Meanwhile, a corresponding saturation state is obtained in vacuum.[1,8] On the other hand, as the dielectric surface is heated by electron impact, an adsorbed or evaporated gas layer builds up above the surface. Ultimately, plasma ionization breakdown can occur and cut off the power transmission, damaging the device.[9–14] Therefore, reducing the multipactor process near the rf window surface is the essential step to improve the breakdown threshold and device performance.[5,15]

TiN coatings on the window were first adopted to decrease effective SEY.[16,17] Modifying the window geometry, such as periodic grooves on the window surface in rectangular or triangular shape, were later shown to further reduce multipactor by changing the impact energies of electrons.[18–22] However, the effect is limited. Applying an external dc electric field pointing into the dielectric window was also experimentally shown to improve the multipactor discharge threshold by decreasing the electron flight time and hence decreasing the impact energy.[23–25] An external dc magnetic field parallel to the surface and perpendicular to the rf electric field, with the electron gyrofrequency close to the rf frequency, was also suggested to change the electron flight trajectories and reduce the effective SEY to be lower than unity.[26–29] These methods require the modification of the existing structure of microwave devices and involve new materials, which increase the cost of the devices and sometimes make the system unacceptably heavy,[29] especially for space-based communication systems. In this work, we proposed a Gaussian-type transverse electric field waveform near the window surface to highly reduce the multipactor discharge at fixed input power by performing particle-in-cell (PIC) and Monte-Carlo (MC) simulations.

II. BRIEF DESCRIPTION OF SIMULATION

In the current work, we consider a multipactor discharge on the vacuum side near a dielectric window surface. The surface is assumed to be dull, with surface smoothness factor $k_s = 1$ and maximum SEY $\delta_{max0} = 2.0$ at normal incidence at the impact energy of $E_{max0} = 400.0$ eV, close to SiO_2 materials. We separately applied PIC and MC simulations to investigate the multipactor suppression near a single window surface. In PIC simulations, a large number of charged superparticles with a fixed weight are considered, the motion of charged particles is treated in one dimension normal to the dielectric surface, and the velocities have three components. The space charge effect, as well as the normal restoring field induced by the positive charge on the surface, is self-consistently considered. More details could be found in our previous paper.[30]

For PIC simulations in this work, the simulation domain has a length of 1 mm from the window surface to the vacuum side for the sinusoidal waveform and Gaussian-type waveform at $\Delta\tau > 0.1T$ and a length of 5 mm for $\Delta\tau < 0.1T$, where $\Delta\tau$ and T are the half-peak width and the period of the input electric field, respectively [Eq. (3)]. It is kept much larger than the typical multipactor length, which is usually tens of microns. At the window surface side, the primary electrons flying in the vacuum can return to the surface and induce secondary electron emission. The secondary electron yield depends on the incident electron energy and angle, and it is described by the well-known Vaughn's empirical formula.[31] The emission energy E_0 and emission angle ϕ of the secondary electrons from the dielectric surface are given by the following distributions:[32]

$$f(E_0) = \frac{E_0}{E_{0m}^2} e^{-E_0/E_{0m}}, \tag{1}$$

$$g(\phi) = \frac{1}{2}\sin(\phi), \tag{2}$$

where E_{0m} is on the order of the work function of the dielectric window materials, which is about unit electron volt. In this work, we assume E_{0m} to be 1 eV. The mean emission energy is 2 eV. The boundary of the Poisson equation has a normal electric field of $E_{x,wall} = \sigma_{wall}/\epsilon_0$, with ϵ_0 being the vacuum dielectric constant and σ_{wall} being the positive surface charge density on the dielectric wall. Due to the restoring field and large enough simulation domain, all the electrons are constrained near the surface and could not escape from the computation region. The other boundary is grounded. In addition, 8000 and 40 000 uniform grids are used for 1 mm and 5 mm simulation domains, respectively. The size of the cell (Δx) and time step (Δt) are chosen to satisfy the convergence condition $\max\{v_x \Delta t\} < \Delta x$, where v_x is the electron velocity in the normal direction and Δx resolves the Debye length. The time step is fixed at 10^{-14} s.

In the MC simulation, two hundred macroparticles were traced, and upon impact of each macroparticle, the charge and mass of this macroparticle and the normal electric field are updated according to the SEY and Gauss's law.[33]

We apply a Gaussian type electric field at a repetition frequency of 1 GHz,

$$E(t) = E_G\{\exp[-\beta(t-t_1)^2] - \exp[-\beta(t-t_2)^2]\}, \quad nT \le t < (n+1)T, \tag{3}$$

where E_G is the electric field amplitude and $t_1 = (n+0.25)T$ and $t_2 = (n+0.75)T$, with n being an integer number and T being the repetition period, are the time of the field maximum and minimum, respectively. β is a parameter controlling the shape of the electric field. We can express the pulse width in terms of the full-width half-maximum (and/or half-minimum) of the Gaussian profile, $\Delta\tau = 2\sqrt{\ln 2/\beta}$. The half peak widths, $\Delta\tau$, used here are in the range of 0.01–0.15 T. The transmission power in the Gaussian-type electric field is set to that of the sinusoidal electric field, satisfying the following equation:

$$\int_0^T |E(t)|^2 dt = \int_0^T |E_{sin}\ \sin(\omega_1 t)|^2 dt, \tag{4}$$

where $E_{sin} = 3 \times 10^6$ V/m is the amplitude of the sin-type electric field, and $\omega_1 = 2\pi/T$. The right-hand side gives the practical transmission power per unit area, $\bar{P} = c\epsilon_0 |E_{sin}|^2/2$, i.e., 1.2×10^{10} W/m^2, with c and ϵ_0 being the speed of light and dielectric constant in vacuum, respectively. For a given half peak width $\Delta\tau$, the corresponding amplitudes, E_G, is self-consistently calculated.

III. RESULTS AND DISCUSSION

A. Multipactor suppression and physical mechanism

The sinusoidal and Gaussian electric field waveforms are shown in Fig. 1(a). The black line in Fig. 1(b) shows the normalized amplitudes E_G/E_{sin} vs half peak width $\Delta\tau$. Decreasing the half peak width gives a narrower pulse shape, resulting in a larger amplitude due to the fixed transmission power. The time-averaged positive charge density on the dielectric wall is given by the blue circle line from PIC simulations, where the space charge effect is self-consistently considered, and more details can be found in our previous papers.[10,30] We can see that the time-averaged positive charge density on the surface rapidly decreases first and then slowly decreases upon reducing the half peak width from 0.15 to 0.01 by an order of magnitude, implying that the multipactor discharges could be suppressed by adjusting the half peak width.

The significantly suppressed multipactor discharge is also validated by an independent MC simulation as shown in Fig. 1(b) (blue x line), the same conclusion is obtained. The differences in the absolute values in Fig. 1(b) can be due to the inclusion (absence) of space charge in PIC (MC) simulations. Iqbal *et al.* state[33] that in a realistic case with the space charge effect, the particles in flight at higher altitudes experience lower levels of the normal electric field than the particles in flight at lower altitudes. As a result, their flight times increase, allowing them to gain more energy from the rf electric field while in flight. Therefore, their impact energy is larger, giving larger SEY. In our PIC simulation result that accounts for the space charge effect, we have found that the larger SEY by the particles with larger flight times increases the time average value of the normal electric field corresponding to the multipactor strength compared to the MC simulation results.

The ratio of total electron number to time-averaged transmission power density (black line) from PIC simulation, $N_e/\bar{P}$, reveals the ability of the specific waveform to induce multipactor, and the incident rf power producing the rf transverse electric field (dashed blue line), $P = c\epsilon_0 E^2(t)$, as a function of time, are plotted in Figs. 2(a)–2(d). $N_e/\bar{P}$ oscillates at twice the fundamental frequency driven by the sinusoidal electric field as shown in Fig. 2(a). For case $\Delta\tau = 0.15T$ in Fig. 2(b), the waveform of the electric field is similar to the sinusoidal electric field, but the peak value around $t = t_1$ and $t = t_2$ is larger. As a

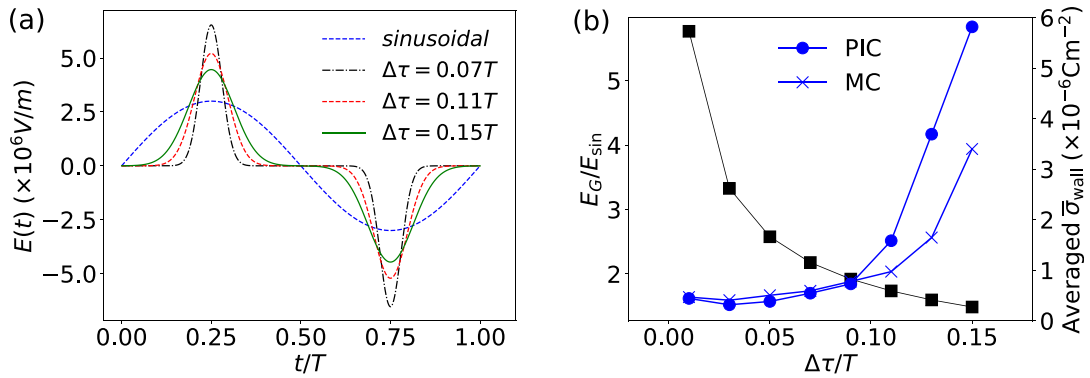

FIG. 1. (a) The temporal electric field of the sinusoidal and Gaussian form for $\Delta\tau = 0.15T$, $0.11T$, and $0.07T$; (b) The amplitude of the Gaussian form electric field (left axis) normalized to 3×10^6 V/m and time-averaged positive charge density (right axis) on the surface wall from the PIC simulation (blue circle line) and MC simulation (blue x line) vs half peak width.

result, the ejected electrons gain more energy near $t = t_1$ and $t = t_2$ and generate more secondary electron emission, resulting in a sharp peak. Decreasing $\Delta\tau$ to $0.11T$, the peak value of $N_e/\bar{P}$ decreases by a factor of 9 and the corresponding time-averaged value almost decreases by a factor of 5, which is consistent with the time-averaged positive charge density in Fig. 1(b). At $\Delta\tau = 0.07T$ and $0.03T$ (not shown), $N_e/\bar{P}$ (also the total electron number) saturates at a smaller value. At the beginning of the multipactor process, even though $N_e/\bar{P}$ overshoots, the

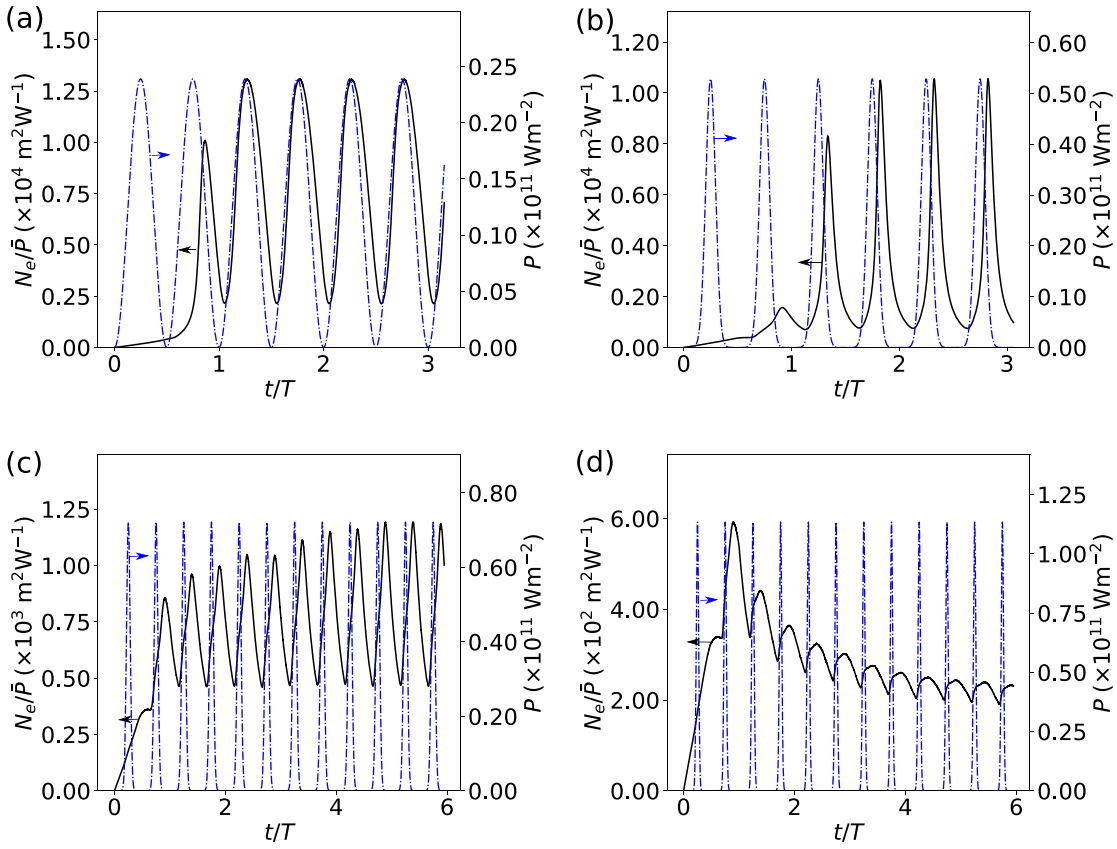

FIG. 2. The ratio of the total electron number to time-averaged wave power density (black line), $N_e/\bar{P}$, from PIC simulations and the instantaneous rf power density exciting the transverse electric field (dashed blue line), P, as a function of time, for the sinusoidal electric field and the Gaussian electric field with various half peak widths $\Delta\tau/T$: (a) sinusoidal electric field, (b) $\Delta\tau/T = 0.15$, (c) $\Delta\tau/T = 0.11$, and (d) $\Delta\tau/T = 0.07$, where $T = 1$ ns is the period.

corresponding peak value is still lower than the case of $\Delta\tau = 0.11T$ by a factor of 2. Comparing the temporal incident rf power, we can see that the peak power density is almost four times higher in the case $\Delta\tau = 0.07T$ than the case of the sinusoidal electric field.

In addition, an interesting phase lag of $N_e/\bar{P}$ vs P in Figs. 2(c) and 2(d) is observed. For the case of the sinusoidal electric field, the electron hop time in the vacuum is much smaller than the rf period, and electrons immediately return to the surface after they obtain energy from the peak rf electric field and bring a peak of secondary electron emissions. Thus, $N_e/\bar{P}$ almost synchronously varies vs P (or electric field). However, for the Gaussian electric field, especially, when the $\Delta\tau$ is small, the reduced normal field lengthens the flight time of electrons, and thus, a significant time delay appears between the maximum energy gain of electrons and the maximum secondary electron emissions. As $\Delta\tau$ decreases, an increased phase lag of $N_e/\bar{P}$ to P is revealed in Figs. 2(c) and 2(d).

Furthermore, the space charge effect-induced spatiotemporal varying normal fields are explicitly revealed in Figs. 3(a)–3(c) for the sinusoidal waveform and Gaussian-type waveform at $\Delta\tau = 0.15T$ and $0.07T$, respectively. The presence of electrons shields the restoring field, giving rise to a decayed normal field toward the vacuum side. The decay is significant within a short length, for example, 30 μm, for the sinusoidal and Gaussian-type waveform at $\Delta\tau = 0.15T$. For these two cases, the restoring field on the surface is so strong that the electrons are constrained with a small space. However, for the case at $\Delta\tau = 0.07T$ in Fig. 3(c), the restoring field at the wall is weaker than the former two cases by a factor of 40, and the electron hop length is relatively long at given initial ejection velocity. In turn, the longer distance is needed to shield the restoring field.

The electrons in the vacuum are driven by the oscillating transverse rf field and the normal restoring field. If the restoring field is assumed to be constant,[5,34] then the electrons would obtain net energy only from the oscillating transverse rf field upon returning to the surface. However, the restoring field as shown in Fig. 3 varies with time. Thus, the electrons also obtain partial energy from the varying restoring field, and the multipactor is dominated by the interaction of the primary electrons and the dielectric surface, where the electron impact energy and angle determine the secondary electron yields.

Figures 4(a)–4(f) show the temporal electron impact energy and angular distribution of primary electrons in the saturation state for the sinusoidal and Gaussian electric field at $\Delta\tau = 0.15T$ and $0.07T$, and the corresponding temporal waveforms of the transverse electric field given by (3) are also shown in Figs. 4(a)–4(c). Note that the impact angle is the angle of the velocity vector with respect to the surface normal, i.e., the impact angle 0 represents the normal impact. Here, the amplitudes of the electric fields are normalized to the amplitude of the sinusoidal electric field, $E_{\sin}$. The impacting electron distribution in terms of impact energy and angle results in secondary electron emission strength as a function of time, and the induced SEY vs time is also shown in Figs. 4(d)–(f) (white dashed line). For the base case, we can see in Figs. 4(a) and 4(d) that the temporal electron impact energy distribution follows the rf electric field, and almost no electrons strike the surface near the phase $t/T \approx 0$ and $0.5T$ due to the small restoring electric field (indicated by the time-dependent number of electrons in the vacuum, see Fig. 2) and the resulting relatively large flight time. As time goes on, the electrons at low energy [below 20 eV, see Fig. 4(a)] start to impact the surface. Due to the small restoring field, electrons returning to the surface are accelerated primarily in the transverse direction, giving rise to a large impact angle [0.4π–0.5π, see Fig. 4(d)]. These electrons induce an increasing number of secondary electrons, as shown by the white dashed line in Fig. 4(d). Gradually, the rf field approaches its maximum value and largely accelerates the electrons to obtain a higher energy in the direction parallel to the surface. Meanwhile, these electrons are also accelerated by the increased restoring field in the normal direction. Thus, the electron-surface impacts under a small angle (around 0.3π) increase. When the rf fields decrease to have a value near zero at $t/T \approx 0.5$, a very small number of electrons return to the surface similar to the situation at $t/T \approx 0$. The electrons in the vacuum slow down because the rf field changes its sign, reducing the energy absorption. This transition also gives rise to the impacts at low energy as stated above. This process is periodically repeated in the saturation state.

For the case of the Gaussian electric field at $\Delta\tau = 0.15T$, the waveform of the electric field gets relatively sharp with an amplitude higher than the base case by a factor of 1.5, and the temporal energy and narrow angular distribution are shown in Figs. 4(b) and 4(e). The peak values of the impact energy distribution at $t/T = 0.33$ and 0.83 show the maximum relative secondary electron emission yield. Decreasing the half peak width to $\Delta\tau/T = 0.07$ in Figs. 4(c) and 4(f), the impacts at low energy (smaller than 30 eV) occur when the electric field is near zero. However, the impacts at high energy exist over the whole period. According to the absence of low energy impacts near the phase $t/T \approx 0.25$ and 0.75 in Fig. 4(c) and the obvious peak of the angular distribution in Fig. 4(f), we can conclude that the high energy electrons have large impact angles (close to 0.5π, parallel to the surface). The other electrons are accelerated by the restoring field and contribute to an extended impact angle distribution.

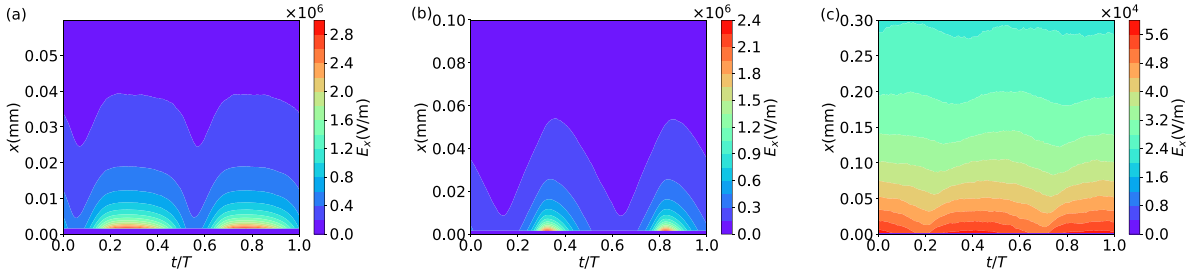

FIG. 3. The spatiotemporal varying normal electric fields for (a) sinusoidal waveform and (b) Gaussian-type waveform $\Delta\tau = 0.15T$ and (c) $\Delta\tau = 0.07T$.

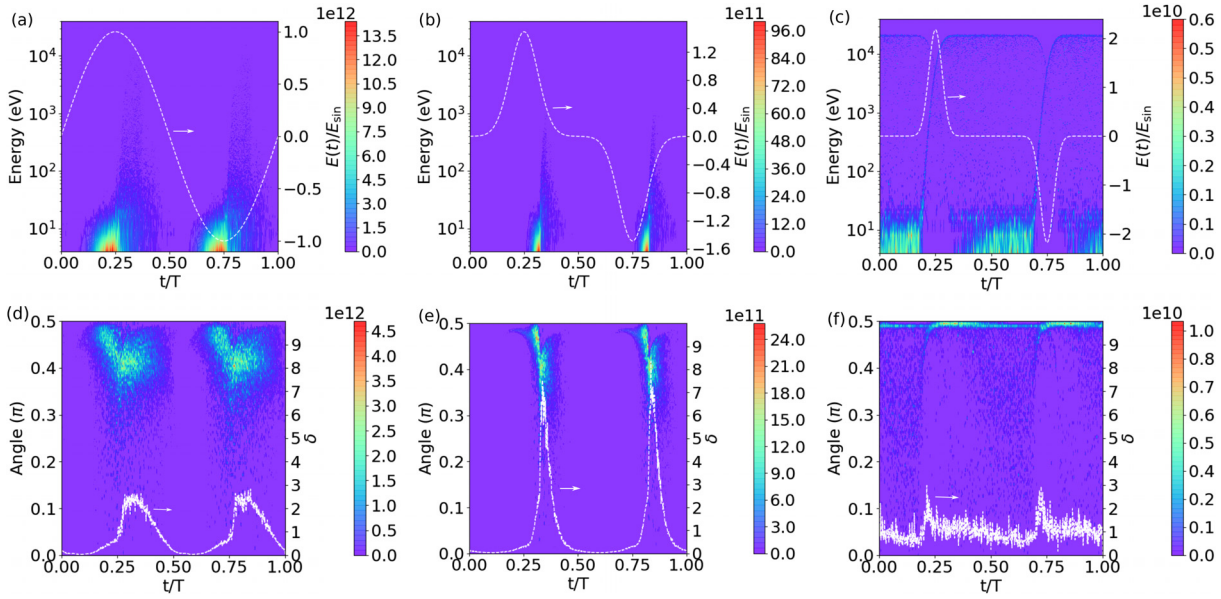

FIG. 4. The number distribution of electrons striking the surface as a function of energy and time in the steady state for (a) sinusoidal electric field, (b) $\Delta\tau = 0.15T$, and (c) $\Delta\tau = 0.07T$, with T being the period of the Gaussian waveform; the white dashed line is the time-dependent driving electric field. The number distribution of particles striking the surface as a function of angle and time for (d) sinusoidal electric field, (e) $\Delta\tau = 0.15T$, and (f) $\Delta\tau = 0.07T$ Gaussian with angle = 0 for the normal to the surface; the white dashed line represents the secondary electron yield for impacts averaged over one rf period for PIC simulations.

Integrating the energy and angle distribution stated above over the whole repetition period separately give the total coupled impact energy-angle distribution in Figs. 5(a)–5(c). The contour lines of the secondary electron yields at the specific angle and energy are labeled by the dashed white lines. We can see that the first crossover, where the secondary electron yield equals unity, relatively weakly depends on the impact angle in the range of 0–0.5π (approximately 35 eV at 0.5π and 45 eV at an angle of 0). However, the second crossover point shows a strong dependence on the impact angle. For the base cases of the sinusoidal electric field and the Gaussian case of $\Delta\tau = 0.15T$ in Figs. 5(a) and 5(b), respectively, the electron impact energy is lower than the second crossover point for any impact angle. However, for the case of $\Delta\tau/T = 0.07$ in Fig. 5(c), the highest impact energy exceeds the second crossover point, giving SEYs below unity. In addition, the transverse electric field is small for most of the period, and the small restoring electric field slightly accelerates the electrons, giving rise to an increasing ratio of impacts at low energy and small impact angles.

To better understand the transit dynamics of the multipactor suppression process at a small half peak width [see $\Delta\tau = 0.07T$ in Fig. 2(d)], Figs. 6(a) and 6(b) show the corresponding impact energy and angle distribution for the initial three cycles. In the beginning, the background electrons induce an electron multipaction process. However, parts of the background electrons in the first period are either less efficiently accelerated by the flat part of the transverse electric field near zero or accelerated by the high peak electric field near $t = 0.25T$ and $t = 0.75T$ to have a high energy, giving a value of impact energy either lower than the first crossover or higher than the second crossover point of the SEY curve as shown in Fig. 5(c). In the beginning of all the simulations, an initially injected electron current from the window representing the background seed electrons exists for the

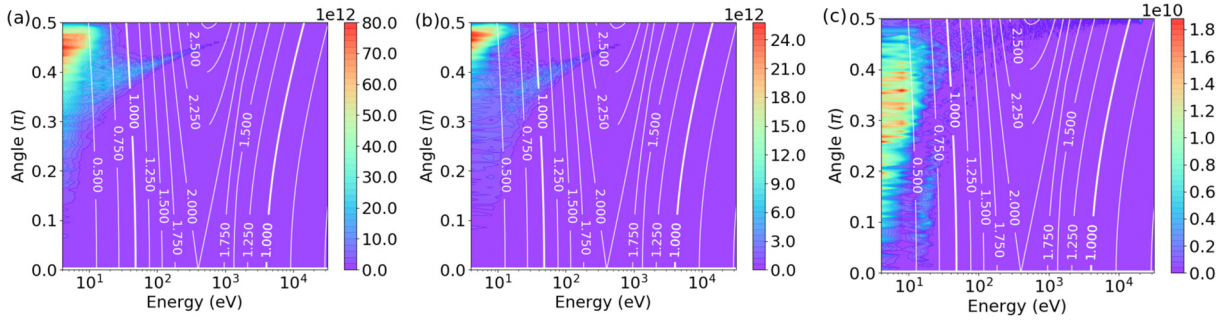

FIG. 5. The number distribution of electrons vs impact energy and angle averaged over the whole period for (a) sinusoidal electric field, (b) $\Delta\tau = 0.15T$, and (c) $\Delta\tau = 0.07T$, with T being the period; the corresponding white contour lines of secondary electron yields are Vaughan's empirical formula[31] for the specific impact energy and angle.

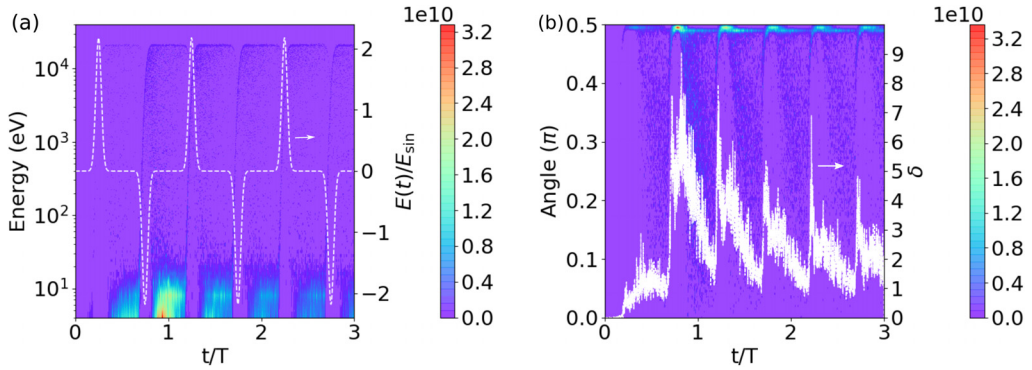

FIG. 6. The number distribution of electrons striking the surface as a function of (a) energy and time and (b) angle and time at $\Delta\tau = 0.07T$ for the initial three periods. The white dashed line represents waveform of the electric field and secondary electron emission yields, respectively.

initial one period.[30] With time going on, the number of generated electrons gradually decreases as shown by the energy and angle distributions, and also revealed by the temporal secondary electron yields, revealing that multipactor is initially reduced in the case of the small half peak width.

B. Generation of the Gaussian-type waveform and frequency spectrum dependent multipactor

In this part, we will discuss the generation of the ideal Gaussian-type waveform. It is well known that the arbitrary periodic signal can be recovered by superimposing multiple frequency sinusoidal signals. The Gaussian-type waveform in Eq. (3) could be written as follows:

$$E(t) = \sum_{m=1}^{2N-1} E_m \cos(\omega t + \theta_m). \tag{5}$$

Here, E_m and θ_m are the amplitude and phase shift of the signal at angular frequency $\omega = m\omega_1 = 2\pi f$, with $f = 1$ GHz being the fundamental frequency, and their values can be analytically given by

$$E_m = \begin{cases} 0 & (m = 0, 2, 4\ldots) \\ \dfrac{4E_G}{T}\sqrt{\dfrac{\pi}{\beta}}e^{-\frac{m^2\omega_1^2}{4\beta}} & (m = 1, 3, 5\ldots) \end{cases} \tag{6}$$

and

$$\theta_m = \begin{cases} -\dfrac{\pi}{2} & (m = 1, 5, 9\ldots) \\ \dfrac{\pi}{2} & (m = 3, 7, 11\ldots). \end{cases} \tag{7}$$

The mathematical derivation is given in the Appendix. Obviously, if m is an even number, then the amplitude of the mth harmonic is zero.

The frequency spectrum of the Gaussian-type waveform, i.e., the amplitude E_m, and the phase shift, θ_m, of the mth harmonic, given in Eqs. (6) and (7), are shown in Figs. 7(a) and 7(b), respectively. As a comparison, the precise numerical calculations by the fftpack library function in python are also given. For half peak widths, $\Delta\tau = 0.07T$, $0.11T$, $0.15T$, the results from Eqs. (6) and (7) are in excellent agreement with the numerical calculation, except some extremely weak amplitudes of even harmonics (less than 0.5% of the odd harmonics) are observed in precisely numerical calculations. These negligible differences are from the approximation of Eq. (A6). We can see that the frequency spectrum has a dominant component of fundamental frequency (f) at large $\Delta\tau$, such as $0.15T$, and the higher frequency ($3f$, $5f$, $7f$) is gradually demanded with decreasing $\Delta\tau$.

Figure 8(a) shows the ideal Gaussian-type waveform ($\Delta\tau = 0.07T$) and waveforms from Eq. (5) by considering the first N terms with $N = 3$, 4, 5. It clearly shows that Eq. (5) gradually

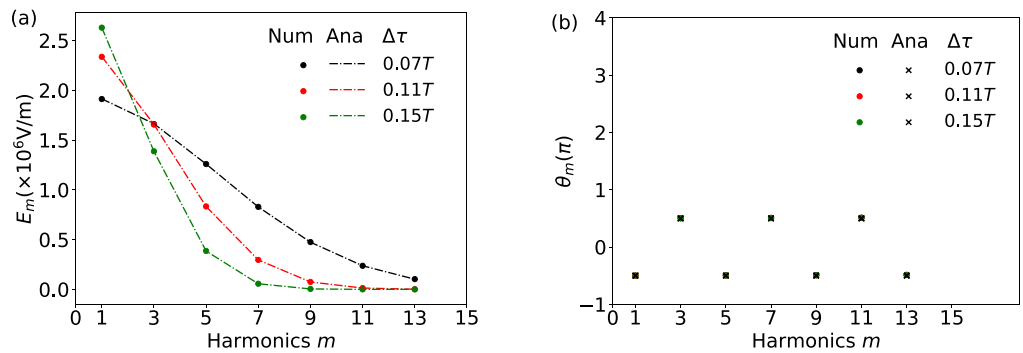

FIG. 7. (a) The amplitudes, E_m, and (b) the phase shift, θ_m, for different half peak widths, $\Delta\tau = 0.07T$, $0.11T$, and $0.15T$ with $T = 1$ ns. "Num" and "Ana" represent the numerical calculation by the fftpack library function in python and analytical expressions in Eqs. (6) and (7), respectively.

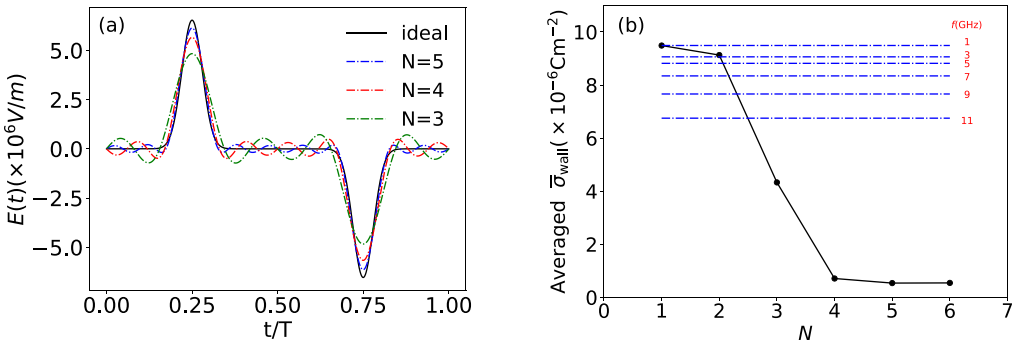

FIG. 8. (a) The ideal Gaussian-type electric field waveform for $\Delta\tau = 0.07T$ given by Eq. (3) and the approximation waveform given by Eq. (5) for $N = 3, 4, 5$; (b) the time-averaged surface positive charge density, $\bar{\sigma}_{\text{wall}}$, vs different waveforms given by Eq. (5) for $N = 1$–6 (circle line), and the blue dashed lines indicate the values of $\bar{\sigma}_{\text{wall}}$ at the same conditions as $N = 1$, except the changed frequency, f, in the range of 1–11 GHz.

approaches ideal waveforms with increasing N. The corresponding averaged surface positive charge density, $\bar{\sigma}_{\text{wall}}$, is given in Fig. 8(b) (circle line) for $N = 1$–6. We can see that the multipactor could be suppressed at $N = 3$ and further significantly suppressed at $N = 4$, whose suppression efficiency is almost equivalent to the ideal Gaussian-type waveform, implying that $N = 4$ is good enough in realistic application. In addition, the values of $\bar{\sigma}_{\text{wall}}$ at the same condition as $N = 1$, except the separately changed frequency (f) in the range of 1–11 GHz, are shown by blue dashed lines in Fig. 8(b). Thus, comparing $\bar{\sigma}_{\text{wall}}$ for $N > 4$ and the blue dashed lines, it can be concluded that the changed shape of waveforms plays a more important role in suppressing multipactor rather than the increased frequency, even though higher frequency also makes multipactor weaker.

IV. CONCLUDING REMARKS AND FUTURE WORK

In this work, we demonstrate that the single-surface multipactor could be significantly suppressed by Gaussian type transverse electric field waveforms instead of general sinusoidal waveforms. This can be applied to increase the breakdown threshold of rf windows in high power microwave transmission devices. The underlying physical regime is clarified by addressing the dynamics of the impact energy and angular distribution of primary electrons. The result at a small half peak width is important because time-averaged input power is fixed and peak power is higher, but multipactor is highly reduced.

Furthermore, we discussed the method to generate a Gaussian-type waveform by superimposing multifrequency signals near the surface. The analytical expressions of the amplitudes and phases for different frequencies are given. The more sinusoidal terms considered, the more precise Gaussian-type waveform can be obtained. However, to get the same multipactor suppression efficiency by the Gaussian-type waveform, only a few low frequency harmonics, along with the fundamental frequency signal, are needed. In more general terms, the attendance of customized weak higher frequency components, shaping the total waveform close to the Gaussian-type waveform, can help significantly suppress single-surface multipactor.

In addition, one-dimensional simulations in the direction normal to the surface were conducted. In some cases, certain physical parameters may vary along the transverse direction of the wall. Full two-dimensional PIC simulations will be conducted in the near future to realize the effects of such a variation. Other types of electric field waveforms, such as rectangular and triangular waveforms, will also be done.

ACKNOWLEDGMENTS

This work was funded by the Air Force Office of Scientific Research (AFOSR) MURI Grant No. FA9550-18-1-0062.

APPENDIX: ANALYTICAL FREQUENCY SPECTRUM AND PHASE FOR THE GAUSSIAN-TYPE WAVEFORM

The ideal Gaussian-type waveform could be recovered by superimposing multiple carrier frequency signals, and in this appendix, we derived the analytical expression of the amplitudes and phases for different harmonic components.

As given in Eq. (3), the periodic Gaussian waveform electric field is

$$E(t) = E_G\{\exp[-\beta(t-t_1)^2] - \exp[-\beta(t-t_2)^2]\}, \quad 0 \le t < T, \tag{A1}$$

which can also be expressed by

$$E(t) = E_0 + \sum_{m=1}^{+\infty} E_m \cos(m\omega_1 t + \theta_m) = \sum_{m=-\infty}^{+\infty} F_m(\omega) e^{jm\omega_1 t}, \tag{A2}$$

where $\omega = m\omega_1$ is the frequency of the mth harmonic, with ω_1 being the fundamental angular frequency, $F_m(\omega)$ is the corresponding complex amplitude, and $t_1 = T/4$ and $t_2 = 3T/4$, with T being the rf period as defined in Eq. (3). Thus, calculating $F_m(\omega)$ gives E_m and θ_m, respectively. Obviously, we have

$$F_m(\omega) = \frac{1}{T}\int_0^T E(t) e^{-j\omega t} dt. \tag{A3}$$

Substituting Eq. (A1) into Eq. (A3) yields

$$F_m(\omega) = \frac{E_G}{T}\int_0^T e^{-\beta(t-t_1)^2} e^{-j\omega t} dt - \frac{E_G}{T}\int_0^T e^{-\beta(t-t_2)^2} e^{-j\omega t} dt. \tag{A4}$$

The first term at the right-hand side is

$$\frac{E_G}{T}\int_0^T e^{-\beta(t-t_1)^2}e^{-j\omega t}dt = \frac{E_G}{T}e^{-j\omega t_1}e^{-\frac{\omega^2}{4\beta}}\int_0^T e^{-\beta(t-t_1+\frac{j\omega}{2\beta})^2}dt. \quad \text{(A5)}$$

In addition, according to the relationship between the shape factor, β, and the half peak width, $\Delta\tau$, we have

$$\frac{j\omega}{2\beta} = \frac{j\pi m\alpha^2 T}{4\ln 2}, \quad \text{(A6)}$$

with $\alpha = \Delta\tau/T$ and m being the harmonic number. If we consider the main harmonics, then m is a small integer number. For the narrow waveform shape, $\alpha \ll 1$, then $|j\pi m\alpha^2/\ln 2| \ll 1$, i.e., $|j\omega/2\beta| \ll t_1$. As a result, the function $e^{[-\beta(t-t_1+j\omega/2\beta)^2]}$ is approximately symmetric with $t = t_1$. Furthermore, the resulting integration at the right-hand side of Eq. (A5) yields

$$\int_0^T e^{-\beta(t-t_1+\frac{j\omega}{2\beta})^2}dt \approx \sqrt{\frac{\pi}{\beta}}, \quad \text{(A7)}$$

based on the summing of the integration,

$$\int_{-\infty}^0 e^{-\beta(t-t_1+\frac{j\omega}{2\beta})^2}dt + \int_T^{+\infty} e^{-\beta(t-t_1+\frac{j\omega}{2\beta})^2}dt \approx 0. \quad \text{(A8)}$$

Finally, we obtain the first term at the right-hand side of Eq. (A5) as follows:

$$\frac{E_G}{T}\int_0^T e^{-\beta(t-t_1)^2}e^{-j\omega t}d = \frac{E_G}{T}\sqrt{\frac{\pi}{\beta}}e^{-j\omega t_1}e^{-\frac{\omega^2}{4\beta}}. \quad \text{(A9)}$$

Similarly, the second term at the right-hand side of Eq. (A4) is

$$\frac{E_G}{T}\int_0^T e^{-\beta(t-t_2)^2}e^{-j\omega t}d = \frac{E_G}{T}\sqrt{\frac{\pi}{\beta}}e^{-j\omega t_2}e^{-\frac{\omega^2}{4\beta}}. \quad \text{(A10)}$$

Thus, the complex amplitude in Eq. (A2) or (A3) is

$$F_m(\omega) = \frac{E_G}{T}\sqrt{\frac{\pi}{\beta}}e^{-\frac{m^2\omega_1^2}{4\beta}}(e^{jm\pi/2} - e^{3jm\pi/2}). \quad \text{(A11)}$$

Considering even and odd harmonics, separately,

$$F_m(\omega) = |F_m(\omega)|e^{j\theta_m} = \begin{cases} 0 & (m = 0, 2, 4\ldots), \\ \dfrac{2E_G}{T}\sqrt{\dfrac{\pi}{\beta}}e^{-\frac{m^2\omega_1^2}{4\beta}}e^{j(\frac{1}{2}+m)\pi} & (m = 1, 3, 5\ldots). \end{cases} \quad \text{(A12)}$$

If we consider the phase in the range of $[-\pi, \pi]$, then the phase shift

$$\theta_m = \begin{cases} -\dfrac{\pi}{2} & (m = 1, 5, 9\ldots), \\ \dfrac{\pi}{2} & (m = 3, 7, 11\ldots). \end{cases} \quad \text{(A13)}$$

Considering the symmetry, finally, E_m in Eq. (A2) is

$$E_m = \begin{cases} 0 & (m = 0, 2, 4\ldots), \\ \dfrac{4E_G}{T}\sqrt{\dfrac{\pi}{\beta}}e^{-\frac{m^2\omega_1^2}{4\beta}} & (m = 1, 3, 5\ldots). \end{cases} \quad \text{(A14)}$$

REFERENCES

[1]L.-K. Ang, Y. Y. Lau, R. A. Kishek, and R. M. Gilgenbach, IEEE Trans. Plasma Sci. **26**, 290–295 (1998).
[2]R. A. Kishek and Y. Y. Lau, Phys. Rev. Lett. **75**, 1218 (1995).
[3]R. A. Kishek and Y. Y. Lau, Phys. Plasmas **3**, 1481 (1996).
[4]R. A. Kishek, Y. Y. Lau, and D. Chernin, Phys. Plasmas **4**, 863 (1997).
[5]R. A. Kishek, Y. Y. Lau, L. K. Ang, A. Valfells, and R. M. Gilgenbach, Phys. Plasmas **5**, 2120 (1998).
[6]A. Valfells, J. P. Verboncoeur, and Y. Y. Lau, IEEE Trans. Plasma Sci. **28**, 529–536 (2000).
[7]R. A. Kishek, Phys. Rev. Lett. **108**, 035003 (2012).
[8]S. Riyopoulos, Phys. Plasmas **4**, 1448 (1997).
[9]H. C. Kim and J. P. Verboncoeur, Comput. Phys. Commun. **177**, 118 (2007).
[10]H. C. Kim and J. P. Verboncoeur, Phys. Plasmas **13**, 123506 (2006).
[11]Y. Y. Lau, J. P. Verboncoeur, and H. C. Kim, Appl. Phys. Lett. **89**, 261501 (2006).
[12]K. S. Nam and J. P. Verboncoeur, Appl. Phys. Lett. **93**, 151504 (2008).
[13]S. K. Nam and J. P. Verboncoeur, Appl. Phys. Lett. **92**, 231502 (2008).
[14]S. K. Nam and J. P. Verboncoeur, Comput. Phys. Commun. **180**, 628 (2009).
[15]C. Chang, G. Liu, C. Tang, C. Chen, and J. Fang, Phys. Plasmas **18**, 055702 (2011).
[16]S. Michizono, Y. Saito, S. Yamaguchi, and S. Anami, IEEE Trans. Electr. Insul. **28**, 692 (1993).
[17]Suharyanto, S. Michizono, Y. Saito, Y. Yamano, and S. Kobayashi, Vacuum **81**, 799 (2007).
[18]A. Neuber, G. Edmiston, J. Krile, H. Krompholz, J. Dickens, and M. Kristiansen, IEEE Trans. Magn. **43**, 496 (2007).
[19]G. Edmiston, A. Neuber, H. Krompholz, and J. Krile, J. Appl. Phys. **103**, 063303 (2008).
[20]C. Chang, H. J. Huang, G. Z. Liu, C. H. Chen, Q. Hou, J. Y. Fang, X. X. Zhu, and Y. P. Zhang, J. Appl. Phys. **105**, 123305 (2009).
[21]L. Wu and L. Ang, Phys. Plasmas **14**, 013105 (2007).
[22]C. Chang, G. Z. Liu, H. J. Huang, C. H. Chen, and J. Y. Fang, Phys. Plasmas **16**, 083501 (2009).
[23]P. Oijala and M. Ukkola, Nucl. Instrum. Methods Phys. Res. A **474**, 197 (2001).
[24]O. A. Ivanov, M. A. Lobaev, V. A. Isaev, and A. L. Vikharev, Accel. Beams **13**, 022004 (2010).
[25]J. Foster, M. Thomas, and A. Neuber, J. Appl. Phys. **106**, 063310 (2009).
[26]A. Valfells, L. K. Ang, Y. Y. Lau, and R. M. Gilgenbach, Phys. Plasmas **7**, 750 (2000).
[27]C. Chang, G. Liu, C. Tang, C. Chen, H. Shao, and W. Huang, Appl. Phys. Lett. **96**, 111502 (2010).
[28]G. Cheng and L. Liu, Appl. Phys. Lett. **102**, 243506 (2013).
[29]C. Chang, J. Verboncoeur, S. Tantawi, and C. Jing, J. Appl. Phys. **110**, 063304 (2011).
[30]H. C. Kim and J. P. Verboncoeur, Phys. Plasmas **12**, 123504 (2005).
[31]J. R. M. Vaughan, IEEE Trans. Electron Devices **40**, 830 (1993).
[32]R. A. Kishek and Y. Y. Lau, Phys. Rev. Lett. **80**, 193 (1998).
[33]A. Iqbal, J. Verboncoeur, and P. Zhang, Phys. Plasmas **26**, 024503 (2019).
[34]P. Zhang, Y. Y. Lau, M. Franzi, and R. M. Gilgenbach, Phys. Plasmas **18**, 053508 (2011).